

Softened sp^2 - sp^3 bonding network leads to strong anharmonicity and weak hydrodynamics in graphene+.

Linfeng Yu¹, Ailing Chen¹, Xiaoxia Wang², Huimin Wang², Zhenzhen Qin³, and Guangzhao Qin^{1,*}

¹State Key Laboratory of Advanced Design and Manufacturing for Vehicle Body, College of Mechanical and Vehicle Engineering, Hunan University, Changsha 410082, P. R. China

²Hunan Key Laboratory for Micro-Nano Energy Materials & Device and School of Physics and Optoelectronics, Xiangtan University, Xiangtan 411105, Hunan, China

³School of Physics and Microelectronics, Zhengzhou University, Zhengzhou 450001, China

Abstract:

Graphene+, a novel carbon monolayer with sp^2 - sp^3 hybridization, is recently reported to exhibit graphene-like Dirac properties and unprecedented out-of-plane half-auxetic behavior [Yu *et al*, Cell Reports Physical Science, 3 100790 (2022)]. Herein, from comprehensively *state-of-the-art* first-principles studies, we report the exceptional lattice thermal transport properties of graphene+ driven by the unique sp^2 - sp^3 crystal configuration. At room temperature, the thermal conductivity (κ) of graphene+ is calculated to be ~ 170 W/mK, which is much lower than that of graphene (~ 3170 W/mK). Despite the buckling structure, weak phonon scattering phase space is trapped in graphene+. Thus, the reduction in κ magnitude stems from soft bonding due to the unique sp^2 - sp^3 crystal configuration. Soft bonding suppresses the vibrations of acoustic phonons, which leads to strong anharmonicity and weak phonon hydrodynamics. Further, lower group velocity, relaxation time and smaller phonon mean free path emerge in graphene+, and the significantly decreased κ is achieved. Our study provides fundamental physical insights into the thermal transport properties of graphene+, and it serves as an ideal model to study atomic bonding versus thermal transport properties due to weak scattering phase space.

* Author to whom all correspondence should be addressed. E-Mail: gzqin@hnu.edu.cn

Keywords: graphene+, softened bonding, phonon hydrodynamics, strong anharmonicity.

1. Introduction

Recent decades have witnessed the vigorous development of carbon materials, and lots of excellent carbon materials have been reported, including diamond¹, T-carbon², and others³⁻⁵. In particular, the successful fabrication of graphene opened the door to the world of two-dimensional (2D) materials⁶, which show excellent properties. Typically, graphene is often used as a research benchmark in carbon monolayers due to its outstanding properties, such as electronic Dirac properties⁷, high breaking strength⁸, and ultra-high thermal conductivity (κ)⁹. In addition, the anisotropic negative Poisson's ratio (NPR) behavior can be induced mechanically in graphene¹⁰⁻¹³. Furthermore, extensive efforts have been devoted to searching for promising 2D carbon candidates beyond graphene. For instance, Zhang *et al* found that pure pentagonal rings can form a novel 2D carbon allotrope, namely penta-graphene¹⁴, which serves as an excellent design platform for 2D penta-materials¹⁵⁻¹⁸. Moreover, a series of 2D carbons with outstanding properties have been reported, such as T-graphene¹⁹, Twin-graphene²⁰, SW-graphene²¹, and biphenylene^{22,23}. Abundant configurations enable carbon materials to form a promising candidate library for micro- and nanoelectronic devices. While in practical applications, the understanding of thermal transport is of great significance to the working lifetime and performance of micro-nano electronic devices, which demands for fundamental study. However, despite the boom in carbon materials, insights into thermal transport properties remain challenging because of expensive experimental equipment and computational resources.

With the abundant and diversified bonding configurations in carbon materials, an in-depth understanding of the thermal transport properties in 2D carbon materials is becoming a central issue. For 2D carbon materials, the strong planar sp^2 hybridized C-C bond properties in graphene lead to its ultra-high κ of 3000-5000 W/mK^{9,24,25}. Choudhry *et al.* reported that the reduced κ of graphene allotropes is due to phonon branches folding induced by the superstructure, independent of bond strength²⁶. And T-graphene, D-graphene, and biphenylene have been reported to exhibit distinctive thermal transport behaviors due to diverse sp^2 bonding, with κ being 800, 600, and 166 (254) W/mK,

respectively^{23,26}. However, the sp^3 hybridization effect is not considered in those study. The sp^3 hybridization will induce a strong buckling structure in penta-graphene, which further contributes to the large scattering phase space and low κ (645 W/mK) due to the breaking of out-of-plane symmetry²⁷. Such phenomenon generally occurs in other 2D compounds, such as silicene²⁵, g-B₃N₅²⁸ and other buckling phases^{29,30}. Interestingly, graphene+ violates this rule despite having similar buckling structures and pentagonal rings. The diverse thermal transport behaviors largely originate from the different C-C bond morphology. Except penta-graphene with the sp^2 - sp^3 hybridization, previously reported thermal transport properties of carbon monolayers generally have sp^2 -hybridized bonding configurations. It remains unknown how the complex sp^2 - sp^3 hybrid bonding affect the thermal transport properties.

Recently, a sp^2 - sp^3 hybrid carbon monolayer graphenepplus (graphene+) has been reported possessing an unprecedented novel *out-of-plane* half-auxetic behavior³¹. The novel auxetic behavior caused by the unique crystal configuration of graphene+ beyond graphene is expected to bring more interesting applications and prospects. In addition, in terms of electrical properties, graphene+ also exhibits the outstanding electronic Dirac properties. However, the unknown thermal transport mechanism in graphene+ limits its further development in electronic devices and thermal management applications despite its excellent mechanical and electrical performance. And the hybrid sp^2 - sp^3 bonding in graphene+ is expected to shed light on the fundamental understanding of bonding effect on thermal transport.

In this paper, based on *state-of-the-art* first-principles calculations, we comprehensively explored the thermal transport properties of graphene+ with graphene as a benchmark comparison. One order of magnitude lower κ than graphene and exceptional thermal transport properties is found in graphene+. To reveal the origin, we conduct mode-level images of phonon properties and discuss the effects of lattice dynamics, phonon hydrodynamics, size effects and four-phonon scattering on the thermal transport properties of graphene+. The mechanism as revealed in this study is expected to provide an answer to the open question how the atom bonding affect thermal transport, which would promote the

applications of graphene+ and other carbon materials in electronics with high performance thermal management.

2. Computational Methodology

All first-principles calculations are performed with the aid of the Vienna *ab initio* simulation package (VASP)^{32,33} based on density functional theory (DFT). The Perdew–Burke–Ernzerhof (PBE)³⁴ is used to describe the correlation between electrons. The kinetic energy cutoff of 1000eV is selected to expand the wave functions in plane-wave basis set. A Monkhorst-Pack³⁵ q -mesh of $9 \times 9 \times 1$ ($15 \times 15 \times 1$) is used to optimize the crystal structure for graphene+ (graphene) until the accuracy of 10^{-6} eV for energy convergence and 10^{-5} eV/Å for the Hellmann-Feynman force convergence. The $2 \times 2 \times 1$ ($5 \times 5 \times 1$) supercell with $2 \times 2 \times 1$ q -mesh to calculate second-order and third-order force constants for graphene+ (graphene). Based on harmonic and anharmonic force constants, the κ is obtained in the ShengBTE³⁶ as

$$\kappa = \kappa_{\alpha\alpha} = \frac{1}{V} \sum_{\lambda} C_{\lambda} v_{\lambda\alpha}^2 \tau_{\lambda\alpha} , \quad (1)$$

where $\tau_{\lambda\alpha}$, C_{λ} , and $v_{\lambda\alpha}$ V are the relaxation time, specific heat capacity and the group velocity for λ mode phonon along α direction, the crystal volume.

3. Results

3.1 Crystal structure and interatomic forces.

The top and side views of the crystal geometry for graphene and graphene+ are shown in Fig. 1(a-d). As a typical sp^2 hybrid carbon monolayer, each carbon atom in graphene forms strong C-C bonds with the other three carbon atoms. The difference is that the five-membered rings are distributed along the diagonal of the square to form a carbon network with sp^2 - sp^3 hybridization. The two sp^3 carbon atoms are in the center of the diagonal line, and the sp^2 carbon atoms form a plus "+" shaped distribution around the sp^3 carbon atoms, thus it is called grapheneplus (graphene+). Since its bonding

deviates from the ideal sp^2 hybridization in graphene, out of plane half-auxetic behavior emerges in graphene+ despite exhibiting Dirac properties³¹. In particular, its thermal transport properties are also expected to exhibit distinct extraordinary properties as a complement and candidate for graphene in the field of thermal management and regulation.

To evaluate the bonding strength and range of graphene+, the normalized force constant trace (NFCT) is calculated. Based on the finite displacement difference method in real space, interatomic force constant can obtain the second derivative of the energy E by:^{37,38}

$$\frac{\partial^2 E}{\partial R_i \partial R_j} = \begin{bmatrix} \frac{\partial^2 E}{\partial R_x \partial R_x} & \frac{\partial^2 E}{\partial R_x \partial R_y} & \frac{\partial^2 E}{\partial R_x \partial R_z} \\ \frac{\partial^2 E}{\partial R_y \partial R_x} & \frac{\partial^2 E}{\partial R_y \partial R_y} & \frac{\partial^2 E}{\partial R_y \partial R_z} \\ \frac{\partial^2 E}{\partial R_z \partial R_x} & \frac{\partial^2 E}{\partial R_z \partial R_y} & \frac{\partial^2 E}{\partial R_z \partial R_z} \end{bmatrix}, \quad (2)$$

where R_α represents the position of the atom along the α direction. The force constant trace (FCT) is able to assess the stiffness of atomic bonding regardless of its atomic coordinates and crystal geometry. Further, NFCT are calculated to assess the relative strength of the atomic bonding for atoms with different spacing, thereby further determine their interaction range:³⁷

$$\text{FCT} = \frac{\partial^2 E}{\partial R_x \partial R_x} + \frac{\partial^2 E}{\partial R_y \partial R_y} + \frac{\partial^2 E}{\partial R_z \partial R_z}, \quad (3)$$

$$\text{NFCT} = \frac{\frac{\partial^2 E}{\partial R_{0,x} \partial R_{n,x}} + \frac{\partial^2 E}{\partial R_{0,y} \partial R_{n,y}} + \frac{\partial^2 E}{\partial R_{0,z} \partial R_{n,z}}}{\frac{\partial^2 E}{\partial R_{0,x} \partial R_{0,x}} + \frac{\partial^2 E}{\partial R_{0,y} \partial R_{0,y}} + \frac{\partial^2 E}{\partial R_{0,z} \partial R_{0,z}}}, \quad (4)$$

where $\frac{\partial^2 E}{\partial R_{i,x} \partial R_{j,\alpha}}$ denotes the harmonic force constant of the interaction between the i^{th} atom and the j^{th} atom along the x direction. When $i=j=0$, $\frac{\partial^2 E}{\partial R_{i,x} \partial R_{j,\alpha}}$ represents the self-interaction force constant along the α direction. Correspondingly, when $i=0, j=n$, it represents the force constant of the atom of the n^{th} nearest neighbor relative to the initial (labeled "0") atom. The cutoff distance-dependent normalized trace behavior enables the evaluation of long-range interactions between atoms, which are prevalent

in rock-salt structures with resonant bonding, such as bulk PbX (X=S, Se, and Te) and monolayer black phosphorene^{37,39-42}.

According to Equ. (4), the result of the NFCT for graphene+ is plotted in Fig. 1(e). When the cutoff radius (r^{cutoff}) of atoms exceeds 2.5 Å, the NFCT values display obvious convergence. As r^{cutoff} increases, the NFCT do not change significantly, especially when the r^{cutoff} is larger than 4 Å, implying that weak long-range interactions in graphene+. This be because the introduction of sp^3 hybridization destroys the original cyclic π bond to form a brand-new bonding morphology while the ring-shaped large π bond induce a long-range resonance in graphene³⁵. In addition, the r^{cutoff} -dependent behavior of κ also suggests weak long-range interactions as shown in the inset of Fig. 1(e) and the light blue shading means a 10% error area relative to the κ at $r^{\text{cutoff}} = 5.4$ Å. The slight error may come from the oscillations caused by the initial guess of the charge density in density functional theory. Thus, in order to obtain a satisfactory and strictly convergent κ , 5.4 Å is selected as the final r^{cutoff} to prevent relatively weak anharmonic effects that are not included.

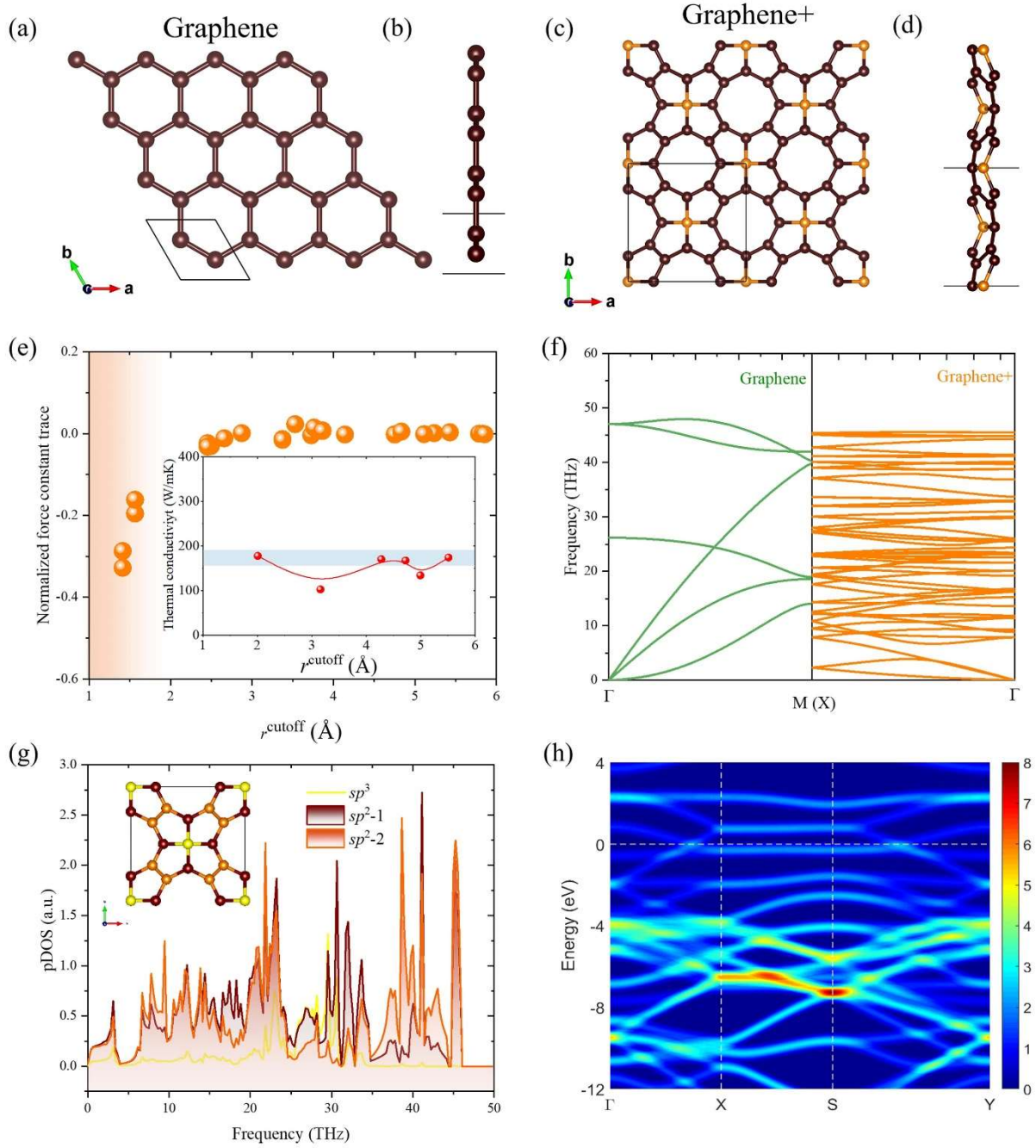


Figure 1. (a) Top and (b) side views for Graphene. (c) Top and (d) side views for Graphene+. (e) Normalized force constant trace (NFCT) and the insert is that thermal conductivity as a function of cutoff radius (r^{cutoff} in Å) for graphene+. (f) Phonon dispersion of graphene and graphene+. (g) The

partial density of states ($pDOS$) of graphene+. (h) Inhomogeneous electron distribution in the energy bands of graphene+.

3.2 Competitive mechanism of lattice dynamics

Further, we evaluate the lattice dynamics and related thermal transport properties in graphene and graphene+ based on phonon dispersion, which are plotted in Fig. 1(f). Similar to graphene, Almost the same phonon vibrational frequency range (0-50 THz) is manifested in the phonon dispersion of graphene and graphene+. However, more complex phonon dispersion appears in graphene+ due to varying geometric crystals and atomic numbers. Notably, the concentrated phonon bands appear flatter in the phonon dispersion, creating a phonon beam-like effect⁴³. In the phonon beam effect, the small gap between the phonon bands makes it difficult for three phonons with similar frequencies to be scattered, whether absorbed or reflected²⁹.

Although the phonon beam effect can effectively reduce the phonon scattering phase space and improve κ , the three acoustic phonon branches at low frequencies are depressed below 10 THz due to due to the substantial filling of the phonon band. A competing mechanism arises between the phonon beam and softened phonons. The softening of the phonon mode implies a weakening of the sp^2 - sp^3 bonding, which can be measured by the change in mechanical properties, thus the Young's modulus E of 120 N/m for graphene+ is much lower than graphene of 320-350 N/m³¹. The E describes the physical quantity of a solid material's ability to resist deformation, and its decrease laterally exhibits softening of the bond. Fig. 1 (g) further reveals the contribution of sp^2 and sp^3 carbon atoms to the phonon partial density of states ($pDOS$). The sp^2 carbon atomic vibrations have a significantly higher density of states peak at 0-10 THz while the sp^3 carbon atoms mainly contribute to the phonon vibrational frequency range of 20-35 THz. However, the κ is mainly contributed by phonons in the 0-10 THz frequency range [Fig. 3(e)], which comes from the phonons of the sp^2 carbon atomic vibrations. This is because sp^3 hybridization will have relatively weak bonding to soften the phonon mode and contribute to lower κ . Weak bonding can gain direct insight from the distribution of electrons in the energy bands as shown

in in Fig. 1(h). Compared to pure sp^2 hybridization in graphene, the electrons in graphene+ are more unevenly distributed across orbitals, more likely to provide more anharmonicity.

3.3 Thermal conductivity

To further explore the effect of sp^2 - sp^3 bonding on thermal transport properties, the temperature-dependent behavior of the κ for graphene+ and graphene is obtained as shown in Fig. 2(a). The κ based on the iterative (ITE) method is ~ 170 and ~ 3170 W/mK for graphene+ and graphene, respectively. The κ of graphene is in good agreement with the experimental and theoretical results of 3000-5000 W/mK^{9,24,44}. The κ of graphene+ is an order of magnitude lower than graphene, and also lower than well-known high-conductivity materials such as diamond⁴⁵, cubic boron arsenide (c-BAs)^{43,46-48} and TaN^{49,50}, but still higher than silicene^{30,51}, black phosphorene³⁹, *etc.* The κ calculated by relaxation time approximation (RTA) method is 440 W/mK for graphene, which is almost an order of magnitude difference compared to ITE method. The RTA-based κ is greatly underestimated, revealing graphene has a strong phonon hydrodynamic effect. Unlike graphene, the RTA method relatively weakly underestimates its κ in graphene+. It is about ~ 110 W/mK, 35% lower than iterative κ , implying weak phonon hydrodynamics, which will be discussed in detail in Sec. 3.5.

The Bonn-Einstein statistical distribution is followed by phonons³⁶, and it changes κ in the system by changing the specific heat capacity and relaxation time with temperature. Hence, the κ followed a decreasing trend with the increasing temperature as shown in Fig. 2(a). Further, the percentage contributions of different phonon branches to the total κ are shown in Fig. 2(b) and (c) for graphene + and graphene, where FA, TA, and LA represent the flexible, transverse and longitudinal acoustic branch at low frequencies respectively, and Opt represents the sum of the optical phonon branches. It is well known that graphene is a 2D material with κ strongly dominated by FA branch. In the temperature range of 200–800 K, the κ is mainly contributed by the FA branch phonons, which almost exceeds 50%. Especially at room temperature, the percentage contribution of the FA branch exceeds 80%, which is consistent with previous studies^{25,52}. In addition, the contribution of TA to κ in graphene increases slightly with temperature, but it is not enough to completely dominate the κ . As for the optical

branch, it contributes little to the κ . Similarly, the FA branch also occupies a slightly larger contribution compared to the other branches in graphene+. At room temperature, it exceeds 50%, almost decisive for κ , but still weaker than that of graphene. Differently, the contribution of the optical branch will have a larger increase with increasing temperature. At 800K, the optical branches contribute almost as much as the FA branch (~40%). The enhancement of optical phonon branching helps graphene+ dissipate heat at high temperatures^{53,54}. Importantly, for most 2D materials, the acoustic branch phonons tend to dominate the κ ^{29,30}, and thus the κ of graphene+ is an order of magnitude lower than that of graphene, largely because the contribution of the acoustic phonon branches (especially the FA branch) is significantly reduced.

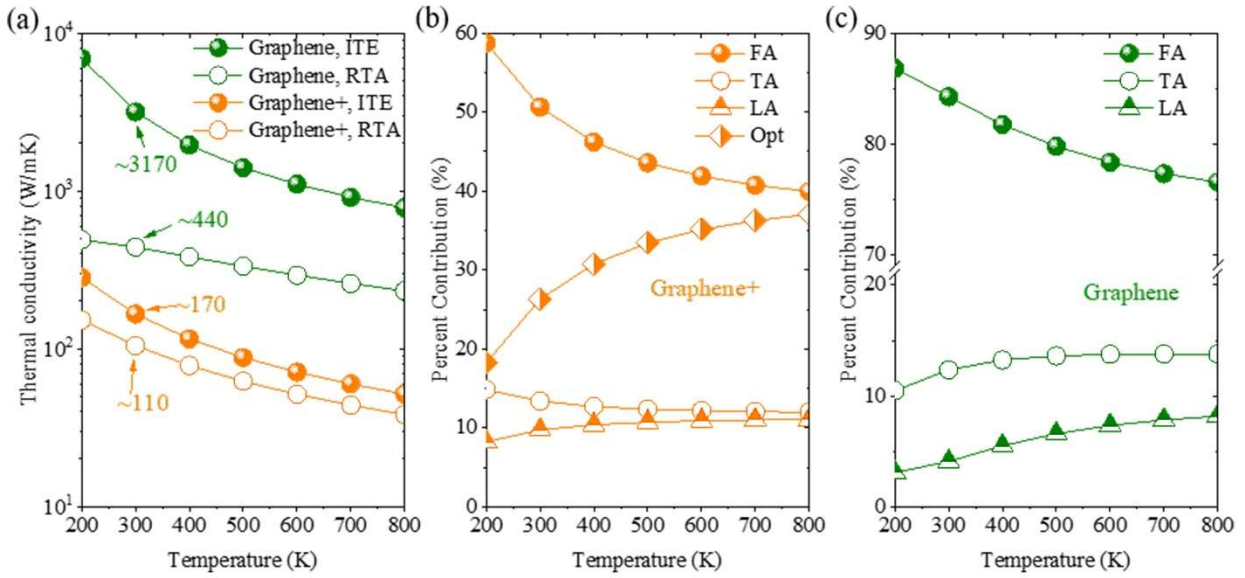


Figure 2. Thermal transport properties as a function of temperature. (a) Lattice thermal conductivity of graphene+ and graphene as a function of temperature. The percentage contribution of each phonon branch to thermal conductivity as a function of temperature for (b) graphene+ and (c) graphene.

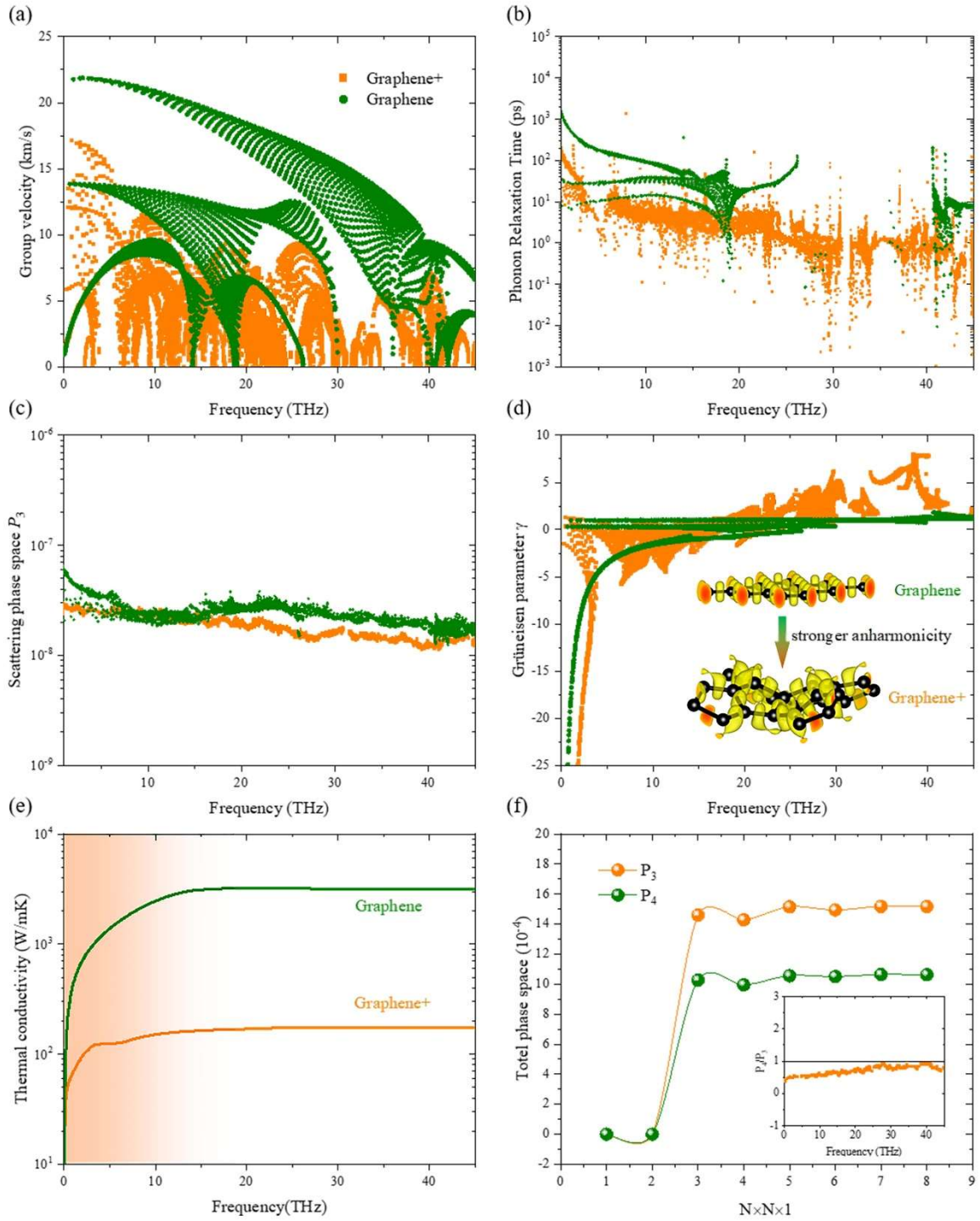


Figure 3. The mode-level (a) group velocity, (b) relaxation time, (c) scattering phase space, and (d) Grüneisen parameter at 300 K. (e) Cumulative thermal conductivity with frequency. (f) Comparison of the three- and four-phonon scattering phase spaces of graphene+. The insert is the ratio of the scattering phase space for three- to four-phonon processes for graphene+.

3.4 Phonon properties

To further reveal the origin of the large reduction in the κ of graphene+, the phonon properties of different modes over the entire frequency vibrational range are comprehensively investigated. The group velocity is derived from the derivation of the phonon dispersion with respect to the phonon wavenumber:

$$v = \frac{\partial \omega}{\partial q}, \quad (5)$$

The phonon relaxation time is derived from the reciprocal of its scattering rate, *i.e.*, $\Gamma = \frac{1}{\tau}$. Based on Matthiessen's rule⁵⁵, summing the scattering rates of different scattering events gives the total scattering rate as follows:

$$\frac{1}{\tau(\vec{q}, p)} = \frac{1}{\tau^{anh}(\vec{q}, p)} + \frac{1}{\tau^{iso}(\vec{q}, p)} + \frac{1}{\tau^B(\vec{q}, p)}, \quad (4)$$

where $1/\tau^{anh}$, $1/\tau^{iso}$, and $1/\tau^B$ are anharmonic (three-phonon), isotopic, and boundary scattering, respectively.

The results of mode-level phonon properties are plotted in Fig. 3. The group velocity measures the speed of phonons in thermal transport, and higher group velocity generally means higher κ . As shown in Fig. 3(a), the group velocity of graphene is also much higher than that of graphene+. Note that the highest group velocity of graphene+ is lower than 20 km/s while graphene is higher than it during 0-10THz. In addition, the group velocity of phonons with frequencies of 0-10 THz in graphene increases rapidly and is generally higher than 5 km/s, but a similar phenomenon is not observed in graphene+, which is caused by the strong softening of the FA branch in graphene+.

As shown in Fig. 3(b), the relaxation time of graphene is much higher than that of graphene+, which is almost an order of magnitude higher. Especially in the range from 0 to 7 THz, the relaxation time of graphene+ tends to decrease sharply, which makes the relaxation time of graphene+ nearly two orders of magnitude lower than that of graphene. This means that there is strong phonon-phonon scattering in the low frequency region of graphene+. In order to measure phonon-phonon scattering,

the mode-level scattering phase space and the Grüneisen parameters are provided in Fig. 3(c) and (d). Commonly, buckling structures tend to have larger scattering phase spaces^{29,56}, which allow for easier scattering between phonons. For example, silicene has a lower κ largely due to the fact that the out-of-plane buckling structure breaks the plane symmetry^{56,57}. In addition, penta-graphene is also found to have a larger phase space, which contributes to lower κ ⁴⁴. Interestingly, graphene+ possesses a lower scattering phase space compared with graphene, which may be due to its unique tetragonal symmetry. Thus, the strong phonon-phonon scattering originates from the large Grüneisen parameter due to strong anharmonicity caused by the softened phonon modes, which overcomes the weak scattering phase space and contributes to the large phonon scattering rate. This strong anharmonicity can be intuitively revealed by the 3D electron localization function as shown in the inset of Fig. 3(d), where the inhomogeneous electrons are localized around the carbon atoms in graphene+ while the graphene remains neatly distributed.

The differences in the phonon properties of different modes are finally reflected in the mode-level κ as shown in Fig. 4(a). The cumulative κ of graphene and graphene+ increases rapidly with increasing frequency. When the phonon frequency is 0-10 THz, the κ of graphene increases the fastest, and a larger slope is easily observed. This means that the reason for the reduced κ of graphene+ is the softened acoustic phonons, which is consistent with the result of the previous branch contribution [Fig. 2]. Not only that, we note that the frequency range of the main contribution of κ is the vibrational contribution range of sp^2 atoms[Fig. 1(f)], which means that the sp^3 atoms will suppress the κ of graphene+.

Attentively, the discussion above treats three-phonon scattering as the dominant scattering process. In fact, four-phonon scattering also plays an important role in some specific systems. Typically, in 2013, *Lindsay et al.* reported that c-BAs has an ultrahigh κ of ~ 2200 W/mK at room temperature based on three-phonon scattering⁴³. In 2017, *Ruan et al.* applied four-phonon scattering to c-BAs and found a 36% decrease in the κ ⁵⁸. In 2018, three independent research groups synthesized c-BAs experimentally, and found that the κ of c-BAs is consistent with the results of four phonons⁴⁶⁻⁴⁸, which proves the importance of four phonons in c-BAs. The strong four-phonon scattering is

dominated by the acoustic phonon band decoupled by the wide phonon band gap^{43,43}, leading to larger phase space for four-phonon scattering ($P_4 = 3.9 \times 10^{-3}$) than three-phonon scattering ($P_3 = 3.8 \times 10^{-4}$) in c-BAs. To evaluate the four-phonon effect, the comparison of the P_3 and P_4 as a function of the $N \times N \times 1$ grid is provided in Fig. 3(f). The P_3 after convergence is significantly higher than that of P_4 , which means that P_3 still dominates the thermal transport process in graphene+. In addition, based on the ratio of the P_4 to P_3 to measure the dominance of graphene+ the entire vibrational interval, *i.e.*, P_4/P_3 , as shown in the insert of Fig. 3(f). The overall ratio is below 1, which means that P_3 plays a more important role in phonon thermal transport in the whole phonon vibration process. This weak four-phonon effect is due to the facts that the same atomic mass leads to narrow phonon band gaps compared to the large atomic mass difference between As and B elements in c-BAs, and an intuitive difference can be observed from the phonon dispersion [Fig. 1(d)]. Therefore, the κ based on three-phonon scattering can be considered reasonable.

3.5 Phonon hydrodynamic effect

The finite size causes scattering of phonons and boundaries in the material, which can be further estimated by²⁵:

$$\frac{1}{\tau^B(\vec{q}, p)} = \frac{1-p}{1+p} \frac{|v_\alpha(\vec{q}, p)|}{L}, \quad (6)$$

where $v_\alpha(\vec{q}, p)$ is the group velocity along the α direction. The L represents the size and p is a speculative parameter that measures the fraction of phonons involved in scattering. Here the boundary scattering is assumed to be a completely rough interface based on perfect diffuse scattering, *i.e.*, $p = 0$. Finally, we show the cumulative κ as a function of mean free path (MFP) in Fig. 4(a). Within the ballistic transport of phonons, κ grows L with the size of the system: $\kappa \sim C\nu L$. Phonons with a large MFP tend to be less easily scattered, and it contributes to higher κ . The MFP of graphene+ is about in the range of $10-10^5$ nm, which is lower than that of graphene (10^2-10^5 nm) as a whole. Further, the MFP corresponding to 50% of the cumulative κ is chosen as the representative MFP (rMFP) to measure the effect of size effect on thermal transport. The rMFP of graphene is ~ 1150 nm, which is consistent

with previous predictions²⁵. The rMFP of graphene+ is ~ 300 nm, which is an order of magnitude lower than that of graphene, largely due to its smaller group velocity and relaxation time. Thus, softened bonding results in low rMFPs and narrow MFPs, which are unfavorable for thermal transport.

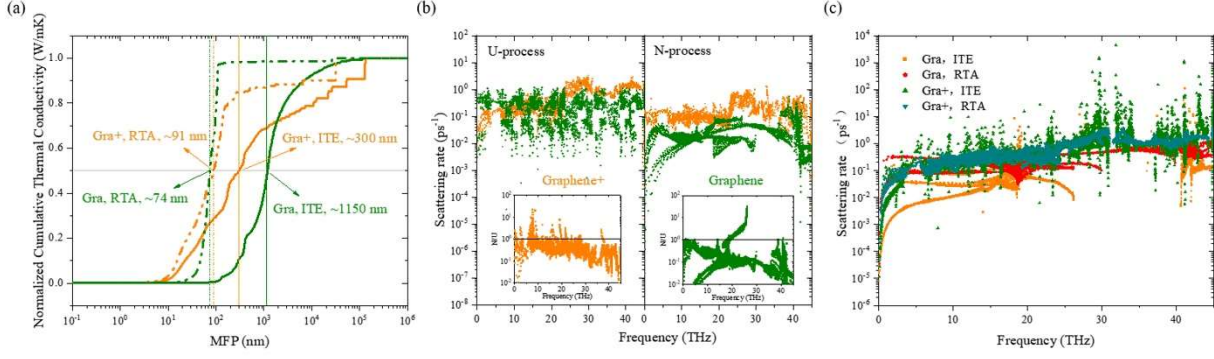


Figure 4. (a) Normalized thermal conductivity as a function of mean free path (MFP). (b) Comparative analysis of N and U processes in graphene+ and graphene. The insert is the ratio of the scattering rates of N to U processes. Orange and green represent graphene+ and graphene, respectively. (c) Comparison of phonon scattering rates based on iterative (ITE) and relaxation time approximation (RTA) methods for graphene+ (Gra+) and graphene (Gra).

The size effect of phonons in graphene is closely related to its phonon hydrodynamics^{59,60}, which can also be captured in transition metal chalcogenides⁶¹. Phonon hydrodynamics means that phonons exhibit fluid-like macroscopic drift motions, namely the momentum-conserving collisions between a large number of phonons as charge carriers lead to the hydrodynamic flow during thermal transport. In such collisions, freezing reduces the typical wavelength of thermally excited phonons, thereby preserving momentum and becoming normal (N) scattering events. When the wave vector generated by scattering between two phonons exceeds the unit vector of the reciprocal lattice, the excess momentum is lost to the underlying lattice. Such phenomena are defined as umklapp (U) scattering events because they require sufficiently large wave vectors. Thus, the phonon hydrodynamics can be evaluated by the collision of the N and the U process. The three-phonon scattering process is determined by the conservation of momentum⁶²:

$$\vec{q} \pm \vec{q}' = \vec{q}'' + \vec{K}. \quad (7)$$

where $\vec{K} = 0$ and $\vec{K} \neq 0$ are N and U processes, respectively.

The quadratic FA branch in graphene leads to the large scattering phase space of normal (N) processes overtaking umklapp (U) processes, which contributes to the strong hydrodynamic effect of the FA mode⁵⁸. In graphene+, the softened sp^2 - sp^3 bond suppresses the acoustic phonon branches, making them flatter, which is a predictably weak hydrodynamic effect. The phonon-phonon scattering rates contributed by N and U are plotted in Fig. 4(c). In both graphene and graphene+, the U process contributes a stronger scattering rate than the N process, which means that the N process has a larger relaxation time and contributes more to κ while the U process contributes less. Note that the contribution of the N process to κ in graphene+ is weaker than that in graphene due to the strong N process scattering rate, which manifests as a weak hydrodynamic effect. Another intuitive evidence of hydrodynamics is the phonon Poiseuille flow, which can be quantified by the exponential power of κ as a function of temperature^{63,64}. By fitting the κ versus temperature relationship $\kappa \sim T^c$, $c = 1.3$ is obtained for graphene+ but $c = 1.8$ is for graphene. A low exponential factor means weak Poiseuille flow, *i.e.*, weak hydrodynamics. In graphene, long-range phonons ensure that phonon scattering is achieved in reciprocal space (N process). In contrary, the reduced MFP tends to make phonons more inclined to complete U process scattering across the Brillouin zone in graphene+. The relative strength of N and U processes can be measured by their mode-level ratio (N/U) as the insert in Fig. 4(c). Obviously, graphene+ (orange insert) exhibits a weaker phonon hydrodynamic effect compared to graphene (green insert), because its N process contributes to a smaller MFP. As shown in Fig. 4(a), the rMFP obtained by the ITE method in graphene+ is two orders of magnitude lower than the RTA, which is one order of magnitude lower than the growth of rMFP in graphene. The RTA method treats N-process phonon collisions as thermal resistance but does not contribute actually. Thus, RTA-based phonon-phonon scattering is severely overestimated in graphene as shown in Fig. 4(c), which leads to a significant underestimation of κ ^{25,28,52}.

To further demonstrate the weak hydrodynamics in the sp^2 - sp^3 network, the κ of several typical 2D carbon allotropes are evaluated based on ITE and RTA methods including penta-graphene (sp^2 - sp^3), biphenylene (sp^2), T-graphene (sp^2). The ratio $\kappa_{\text{ITE}}/\kappa_{\text{RTA}}$ is the ratio of κ of ITE to RTA, and the

higher it means the stronger the hydrodynamics. As shown in Table 1, compared with sp^2 hybridization, the introduction of sp^3 has a stronger negative effect on phonon hydrodynamics due to smaller value $\kappa_{ITE}/\kappa_{RTA}$.

As discussed above, the softened bonding flattens the acoustic phonon branch, leading to strong N process collisions and weak hydrodynamics, which ensures that phonons with small MFP achieve momentum conservation in reciprocal space.

Table 1: Comparison of hydrodynamic effects in different hybridized two-dimensional carbon structures.

	κ_{ITE}	κ_{RTA}	$\kappa_{ITE}/\kappa_{RTA}$	Bond network
Graphene+	170	110	1.56	sp^2 - sp^3
Penta-graphene	437	272	1.61	sp^2 - sp^3
Biphenylene	267 (x)	142 (x)	1.88 (x)	sp^2
	421 (y)	207 (y)	2.03 (y)	
T-graphene	645	243	2.65	sp^2
Graphene	3170	440	7.20	sp^2

3.6 Quantification of weak interatomic bonding

Although the above analysis explains that weak bonding causes strong anharmonics and weak hydrodynamic effects, the weakening sp^2 - sp^3 network bonding is not well quantified. The restoring force of lattice atoms when vibrating near the equilibrium position can be evaluated by the potential well, which reflects the strength of the bonding between atoms^{25,65}. The potential well describes the relationship between the potential energy of the system and the displacement of atoms in positive and negative, and it can be obtained by applying positive and negative strain as shown in Fig. 5(a). At the same potential level, the wider potential well in graphene+ means that it needs more energy to recover to the equilibrium position, which indicates the weak restoring force and atomic bonding in graphene+.

The weak restoring force and bond strength can be further evaluated by the root mean square displacement (MSD), which describes the amplitude of the vibration of the lattice at the equilibrium position and its sensitivity to the potential energy surface. MSD can be obtained by tracking the

evolution of atomic positions in the system with time during molecular dynamics, which is derived by:⁶⁶

$$\text{MSD}(m) = \frac{1}{N_{\text{particles}}} \sum_{i=1}^{N_{\text{particles}}} \frac{1}{N-m} \sum_{k=0}^{N-m-1} (\mathbf{r}_i(k+m) - \mathbf{r}_i(k))^2,$$

where $N_{\text{particles}}$, N , $\mathbf{r}_i(t)$ are the number of atoms in the system, the number of frames in the simulation, and the position of atom i at simulation time t . Considering the weak precision of the empirical potential, *ab initio* molecular dynamics (AIMD) is performed to obtain the MSDs of graphene+ and graphene as shown in Fig. 5(b). The MSD ratio ($\text{MSD}_{\text{gra}}/\text{MSD}_{\text{gra+}}$) of graphene (MSD_{gra}) and graphene+ ($\text{MSD}_{\text{gra+}}$) is also plotted to assess the relative magnitudes within the simulation domain. In the simulations, a larger MSD than graphene is found in graphene+, implying a further deviation. Near the equilibrium position, the energy of atomic vibrations originates from thermal fluctuations ($k_B T$), contributing a deviation, and thus graphene+ requires greater energy for recovery (wider potential well curve).

Based on the above discussion, weaker bonding is identified in graphene+ compared to graphene. The bonding form in graphene+ is more complex, where both sp^2 and sp^3 hybrid carbon atoms exist, while only sp^2 hybrid carbon atoms exist in graphene. Hence, the final step is to determine the relative strength of the bonds between the different hybrid atoms. As shown in Fig. 5(c), the bonding strength between different hybrid atoms in graphene+ is quantified by the integrated Crystal Orbital Hamilton Population (ICOHP)^{67,68}. Smaller ICOHPs indicate larger bonding state occupation by orbital electrons, *i.e.* stronger interatomic bonding. The ICOHP of pure sp^2 bonds in graphene is -10.4 eF. Three types of bonding, sp^2-sp^3 , sp^2-1 , and sp^2-2 , exist in graphene+. The ICOHP of sp^2-sp^3 (-7.8 eF) bond is significantly lower than sp^2 bond in graphene when sp^2-1 (-10.2 eF) and sp^2-2 (-9.3 eF) bonds have a relatively slightly lower difference. Thus, the origin of κ an order of magnitude lower than graphene in graphene+ can be fundamentally explained by softened bonding. In graphene allotropes with the sp^2 hybridized form, the change in κ is independent of the bonding strength, but depends on the band folding induced by the unique phononic crystal structure²⁶. Such an explanation cannot satisfy the

introduction of sp^3 in graphene+. The sp^3 hybridization softens the bonds in graphene+, leading to strong anharmonicity, especially those adjacent to sp^3 -hybridized carbon atoms (weak sp^2 - sp^3 bond).

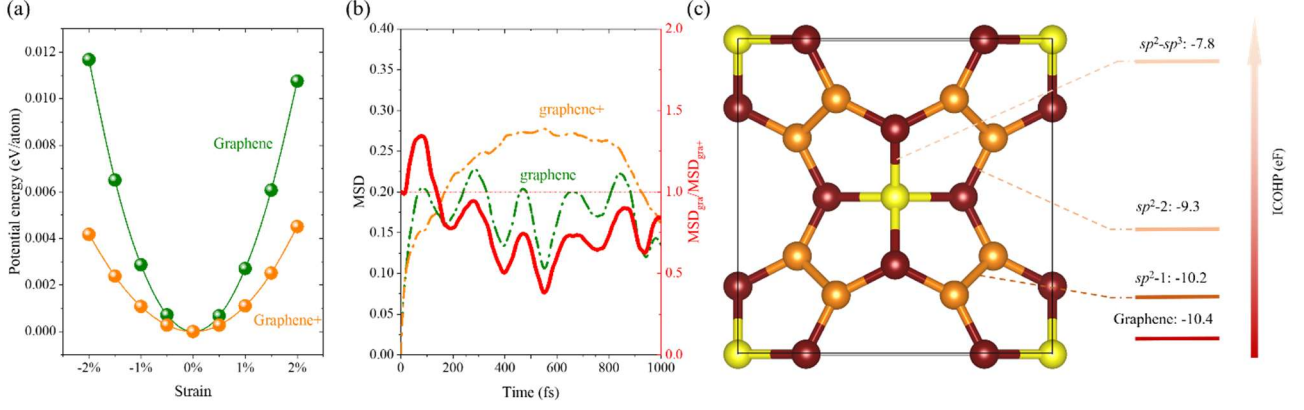


Figure 5. (a) Comparison of potential wells. (b) Root mean square displacement (MSD) based on ab initio analysis dynamics. (c) the integrated Crystal Orbital Hamilton Population (ICOHP) for different hybrid bonds.

4. Conclusion

In summary, we investigate a novel 2D carbon monolayer graphene+ with sp^2 - sp^3 hybrid using *state-of-the-art* first-principles calculations. It is found that the κ of graphene+ is an order of magnitude lower than that of graphene. The origin of low κ can be chalked up to softened bonding in the unique sp^2 - sp^3 crystal network, which suppresses the low-frequency phonons (0-10 THz) that dominate κ . The softened phonon modes induce strong anharmonicity and weak phonon hydrodynamic effects. Based on the analysis of mode-level phonon properties, the strong anharmonicity in graphene+ can be attributed to the large Grüneisen parameter, which overcomes the weak scattering space leading to the low relaxation time, and it can be revealed intuitively through the inhomogeneous electron distribution in the band and electron local functions. Weak hydrodynamic effects are captured phonon collisions based on momentum conservation process (N and U process) and the exponential factor c of the phonon Poiseuille flow. Smaller phonon MFPs ensure weaker N process collisions, and smaller c value indicates weaker phonon Poiseuille flow. Thus stronger phonon-phonon scattering is found in graphene+ due to weaker hydrodynamics. This work provides clear physical insights into the effect of

hybridized sp^2 - sp^3 bonding in graphene+ on thermal transport behaviour. Combined with its unique mechanical auxetic and electronic Dirac properties, an in-depth understanding of the thermal transport behavior of graphene+ can provide effective guidance for electronic devices and related thermal management applications.

ACKNOWLEDGEMENTS

This work is supported by the National Natural Science Foundation of China (Grant No. 52006057), the Fundamental Research Funds for the Central Universities (Grant Nos. 531119200237 and 541109010001), and the State Key Laboratory of Advanced Design and Manufacturing for Vehicle Body at Hunan University (Grant No. 52175013). The numerical calculations in this paper have been done on the supercomputing system of the National Supercomputing Center in Changsha, and the Hefei advanced computing center.

AUTHOR CONTRIBUTIONS

G.Q. supervised the project. L.Y. performed all the calculations and analysis. All the authors contributed to interpreting the results. The paper was writing by L.Y. with contributions from all the authors.

DECLARATION OF INTERESTS

The authors declare no competing interests.

References

1. Ekimov, E. A. *et al.* Superconductivity in diamond. *Nature* **428**, 542–545 (2004).
2. Sheng, X.-L., Yan, Q.-B., Ye, F., Zheng, Q.-R. & Su, G. T-Carbon: A Novel Carbon Allotrope. *Phys. Rev. Lett.* **106**, 155703 (2011).

3. He, C. *et al.* Complex Low Energy Tetrahedral Polymorphs of Group IV Elements from First Principles. *Phys. Rev. Lett.* **121**, 175701 (2018).
4. Yang, X. *et al.* Novel Superhard s p³ Carbon Allotrope from Cold-Compressed C₇₀ Peapods. *Physical review letters* **118**, 245701 (2017).
5. Zhao, Z. *et al.* Novel superhard carbon: C-centered orthorhombic C₈. *Physical review letters* **107**, 215502 (2011).
6. Hashimoto, A., Suenaga, K., Gloter, A., Urita, K. & Iijima, S. Direct evidence for atomic defects in graphene layers. *Nature* **430**, 870–873 (2004).
7. Novoselov, K. S. *et al.* Two-dimensional gas of massless Dirac fermions in graphene. *Nature* **438**, 197–200 (2005).
8. Lee, C., Wei, X., Kysar, J. W. & Hone, J. Measurement of the Elastic Properties and Intrinsic Strength of Monolayer Graphene. *Science* **321**, 385–388 (2008).
9. Chen, S. *et al.* Thermal conductivity of isotopically modified graphene. *Nature Mater* **11**, 203–207 (2012).
10. Qin, Z., Qin, G. & Hu, M. Origin of anisotropic negative Poisson's ratio in graphene. *Nanoscale* **10**, 10365–10370 (2018).
11. Qin, G. & Qin, Z. Negative Poisson's ratio in two-dimensional honeycomb structures. *npj Comput Mater* **6**, 51 (2020).
12. Jiang, J.-W. & Park, H. S. Negative Poisson's Ratio in Single-Layer Graphene Ribbons. *Nano Lett.* **16**, 2657–2662 (2016).
13. Jiang, J.-W., Chang, T., Guo, X. & Park, H. S. Intrinsic Negative Poisson's Ratio for Single-Layer Graphene. *Nano Lett.* **16**, 5286–5290 (2016).
14. Zhang, S. *et al.* Penta-graphene: A new carbon allotrope. *Proceedings of the National Academy of Sciences* **112**, 2372–2377 (2015).
15. Sun, S. *et al.* Flexible, auxetic and strain-tunable two dimensional penta-X₂C family as water splitting photocatalysts with high carrier mobility. *J. Mater. Chem. A* **7**, 7791–7799 (2019).
16. Liu, G., Zeng, Q., Zhu, P., Quhe, R. & Lu, P. Negative Poisson's ratio in monolayer PdSe₂. *Computational Materials Science* **160**, 309–314 (2019).
17. Lv, X. *et al.* Penta-MS₂ (M = Mn, Ni, Cu/Ag and Zn/Cd) monolayers with negative Poisson's ratios and tunable bandgaps as water-splitting photocatalysts. *J. Mater. Chem. A* **9**, 6993–7004 (2021).
18. Tao, W.-L., Zhao, Y.-Q., Zeng, Z.-Y., Chen, X.-R. & Geng, H.-Y. Anisotropic Thermoelectric Materials: Pentagonal PtM₂ (M = S, Se, Te). *ACS Appl. Mater. Interfaces* **13**, 8700–8709 (2021).
19. Liu, Y., Wang, G., Huang, Q., Guo, L. & Chen, X. Structural and Electronic Properties of $\sqrt{3}\sqrt{3}$ Graphene: A Two-Dimensional Carbon Allotrope with Tetrarings. *Phys. Rev. Lett.* **108**, 225505 (2012).
20. Jiang, J.-W. *et al.* Twin graphene: A novel two-dimensional semiconducting carbon allotrope. *Carbon* **118**, 370–375 (2017).
21. Yin, H. *et al.* Stone-Wales graphene: A two-dimensional carbon semimetal with magic stability. *Phys. Rev. B* **99**, 041405 (2019).
22. 范起塘 *et al.* Biphenylene network: A nonbenzenoid carbon allotrope. *Science* **372**, 852–856 (2021).
23. Veeravenkata, H. P. & Jain, A. Density functional theory driven phononic thermal conductivity prediction of biphenylene: A comparison with graphene. *Carbon* **183**, 893–898 (2021).
24. Peng, B. *et al.* The conflicting role of buckled structure in phonon transport of 2D group-IV and group-V materials. *Nanoscale* **9**, 7397–7407 (2017).

25. Qin, Z., Qin, G., Zuo, X., Xiong, Z. & Hu, M. Orbitally driven low thermal conductivity of monolayer gallium nitride (GaN) with planar honeycomb structure: a comparative study. *Nanoscale* **9**, 4295–4309 (2017).
26. Choudhry, U., Yue, S. & Liao, B. Origins of significant reduction of lattice thermal conductivity in graphene allotropes. *Phys. Rev. B* **100**, 165401 (2019).
27. Wang, F. Q., Yu, J., Wang, Q., Kawazoe, Y. & Jena, P. Lattice thermal conductivity of penta-graphene. *Carbon* **105**, 424–429 (2016).
28. Yu, L. *et al.* The synergistic modulation of electronic and geometry structures leads to ultra-low thermal conductivity of graphene-like borides (g-B3X5, X=N, P, As). *arXiv:2202.03622 [cond-mat]* (2022).
29. Yu, L. *et al.* Abnormal enhancement of thermal conductivity by planar structure: A comparative study of graphene-like materials. *International Journal of Thermal Sciences* **174**, 107438 (2022).
30. Peng, B. *et al.* Phonon transport properties of two-dimensional group-IV materials from *ab initio* calculations. *Phys. Rev. B* **94**, 245420 (2016).
31. Yu, L., Qin, Z., Wang, H., Zheng, X. & Qin, G. Half-negative Poisson's ratio in graphene+ with intrinsic Dirac nodal loop. *Cell Reports Physical Science* 100790 (2022) doi:10.1016/j.xcrp.2022.100790.
32. Kresse, G. & Furthmüller, J. "Efficient iterative schemes for *ab initio* total-energy calculations using a plane-wave basis set," *Phys. Rev. B*, vol. 54, pp. 11169-11186. (1996).
33. Kresse, G. & Hafner, J. *Ab initio* molecular-dynamics simulation of the liquid-metal–amorphous-semiconductor transition in germanium. *Phys. Rev. B* **49**, 14251–14269 (1994).
34. Perdew, J. P., Burke, K. & Ernzerhof, M. Generalized Gradient Approximation Made Simple. *Phys. Rev. Lett.* **77**, 3865–3868 (1996).
35. Monkhorst, H. J. & Pack, J. D. Special points for Brillouin-zone integrations. *Phys. Rev. B* **13**, 5188–5192 (1976).
36. Li, W., Carrete, J., A. Katcho, N. & Mingo, N. ShengBTE: A solver of the Boltzmann transport equation for phonons. *Computer Physics Communications* **185**, 1747–1758 (2014).
37. Lee, S. *et al.* Resonant bonding leads to low lattice thermal conductivity. *Nat Commun* **5**, 3525 (2014).
38. Qin, G. & Hu, M. Accelerating evaluation of converged lattice thermal conductivity. *npj Comput Mater* **4**, 3 (2018).
39. Qin, G. *et al.* Resonant bonding driven giant phonon anharmonicity and low thermal conductivity of phosphorene. *Phys. Rev. B* **94**, 165445 (2016).
40. Wang, B.-T., Liu, P.-F., Zheng, J.-J., Yin, W. & Wang, F. First-principles study of superconductivity in the two- and three-dimensional forms of PbTiSe 2 : Suppressed charge density wave in 1 T – TiSe 2. *Phys. Rev. B* **98**, 014514 (2018).
41. Delaire, O. *et al.* Giant anharmonic phonon scattering in PbTe. *Nature Mater* **10**, 614–619 (2011).
42. Shportko, K. *et al.* Resonant bonding in crystalline phase-change materials. *Nature Mater* **7**, 653–658 (2008).
43. Lindsay, L., Broido, D. A. & Reinecke, T. L. First-Principles Determination of Ultrahigh Thermal Conductivity of Boron Arsenide: A Competitor for Diamond? *Phys. Rev. Lett.* **111**, 025901 (2013).
44. Wu, X. *et al.* Hydrogenation of Penta-Graphene Leads to Unexpected Large Improvement in Thermal Conductivity. *Nano Lett.* **16**, 3925–3935 (2016).
45. Slack, G. A. Thermal Conductivity of Pure and Impure Silicon, Silicon Carbide, and Diamond. *Journal of Applied Physics* **35**, 3460–3466 (1964).
46. Li, S. *et al.* High thermal conductivity in cubic boron arsenide crystals. *Science* **361**, 579–581 (2018).

47. Kang, J. S., Li, M., Wu, H., Nguyen, H. & Hu, Y. Experimental observation of high thermal conductivity in boron arsenide. *Science* **361**, 575–578 (2018).
48. Tian, F. *et al.* Unusual high thermal conductivity in boron arsenide bulk crystals. *Science* **361**, 582–585 (2018).
49. Kundu, A. *et al.* Ultrahigh Thermal Conductivity of θ -Phase Tantalum Nitride. *Phys. Rev. Lett.* **126**, 115901 (2021).
50. Guo, S.-D. & Liu, B.-G. Ultrahigh lattice thermal conductivity in topological semimetal TaN caused by a large acoustic-optical gap. *J. Phys.: Condens. Matter* **30**, 105701 (2018).
51. Taheri, A., Da Silva, C. & Amon, C. H. Phonon thermal transport in β -N X (X= P, As, Sb) monolayers: A first-principles study of the interplay between harmonic and anharmonic phonon properties. *Physical Review B* **99**, 235425 (2019).
52. Wang, H. *et al.* Intrinsically low lattice thermal conductivity of monolayer hexagonal aluminum nitride (h-AlN) from first-principles: A comparative study with graphene. *International Journal of Thermal Sciences* **162**, 106772 (2021).
53. Qin, G., Qin, Z., Wang, H. & Hu, M. Anomalously temperature-dependent thermal conductivity of monolayer GaN with large deviations from the traditional $1/T$ law. *Phys. Rev. B* **95**, 195416 (2017).
54. Wang, H., Qin, G., Li, G., Wang, Q. & Hu, M. Low thermal conductivity of monolayer ZnO and its anomalous temperature dependence. *Phys. Chem. Chem. Phys.* **19**, 12882–12889 (2017).
55. Qin, Z., Qin, G., Zuo, X., Xiong, Z. & Hu, M. Orbital driven low thermal conductivity of monolayer gallium nitride (GaN) with planar honeycomb structure: a comparative study. *Nanoscale* **9**, 4295–4309 (2017).
56. Gu, X. & Yang, R. First-principles prediction of phononic thermal conductivity of silicene: A comparison with graphene. *Journal of Applied Physics* **117**, 025102 (2015).
57. Xie, H., Hu, M. & Bao, H. Thermal conductivity of silicene from first-principles. *Appl. Phys. Lett.* **104**, 131906 (2014).
58. Feng, T., Lindsay, L. & Ruan, X. Four-phonon scattering significantly reduces intrinsic thermal conductivity of solids. *Phys. Rev. B* **96**, 161201 (2017).
59. Huberman, S. *et al.* Observation of second sound in graphite at temperatures above 100 K. *Science* **364**, 375–379 (2019).
60. Lee, S., Broido, D., Esfarjani, K. & Chen, G. Hydrodynamic phonon transport in suspended graphene. *Nat Commun* **6**, 6290 (2015).
61. Torres, P., Alvarez, F. X., Cartoixa, X. & Rurali, R. Thermal conductivity and phonon hydrodynamics in transition metal dichalcogenides from first-principles. *2D Mater.* **6**, 035002 (2019).
62. Wang, H. Intrinsically low lattice thermal conductivity of monolayer hexagonal aluminum nitride (h-AlN) from first-principles: A comparative study with graphene. *International Journal of Thermal Sciences* **8** (2021).
63. Gurzhi, R. N. THERMAL CONDUCTIVITY OF DIELECTRICS AND FERRODIELECTRICS AT LOW TEMPERATURES. **4**.
64. Guyer, R. A. & Krumhansl, J. A. Thermal Conductivity, Second Sound, and Phonon Hydrodynamic Phenomena in Nonmetallic Crystals. *Phys. Rev.* **148**, 778–788 (1966).
65. Lou, A., Liu, Q.-B. & Fu, H.-H. Enhanced thermoelectric performance by lone-pair electrons and bond anharmonicity in the two-dimensional Ge₂Y₂ family of materials with Y = N, P, As, or Sb. *Phys. Rev. B* **105**, 075431 (2022).

66. Wang, V., Xu, N., Liu, J.-C., Tang, G. & Geng, W.-T. VASPKIT: A user-friendly interface facilitating high-throughput computing and analysis using VASP code. *Computer Physics Communications* 108033 (2021) doi:10.1016/j.cpc.2021.108033.
67. Dronskowski, R. & Blochl, P. E. Crystal orbital Hamilton populations (COHP): energy-resolved visualization of chemical bonding in solids based on density-functional calculations. *J. Phys. Chem.* **97**, 8617–8624 (1993).
68. Deringer, V. L., Tchougréeff, A. L. & Dronskowski, R. Crystal Orbital Hamilton Population (COHP) Analysis As Projected from Plane-Wave Basis Sets. *J. Phys. Chem. A* **115**, 5461–5466 (2011).